Article

Not peer-reviewed version

TiO_2 Nanocomposite GelMA Film as Wound Dressing: Physicochemical, Structural, Mechanical and Antibacterial Properties

Barbara De Berardis *, Raffaella Pecci, Roberta Morlino, Pietro Ioppolo, Marco Ranaldi, Giovanna Iucci, Alessandro Ferrarini, Giuseppe D'Avenio, Giorgio De Angelis, Maria Grazia Ammendolia *

Posted Date: 25 March 2026

doi: 10.20944/preprints202603.2026.v1

Keywords: GelMA; TiO2NPs; mechanical properties; structural characterization; drug release; antimicrobial activity; wound dressing

 doi:10.20944/preprints202603.2026.v1

Article

TiO_2 Nanocomposite GelMA Film as Wound Dressing: Physicochemical, Structural, Mechanical and Antibacterial Properties

Barbara De Berardis [1,*], Raffaella Pecci [1], Roberta Morlino [2], Pietro Ioppolo [1], Marco Ranaldi [3], Giovanna Iucci [3], Alessandro Ferrarini [3], Giuseppe D'Avenio [1], Giorgio De Angelis [1] and Maria Grazia Ammendolia [1,*]

[1] National Centre Artificial Intelligence and Innovative Technologies for Health, Istituto Superiore di Sanità, Rome (IT)

[2] Environment and Health Department, Istituto Superiore di Sanità, Rome (IT)

[3] Department of Sciences, Roma Tre University, Rome (IT)

* Correspondence: barbara.deberardis@iss.it (B.D.B.); maria.ammendolia@iss.it (M.G.A.)

Abstract

Bacterial infections can delay the wound healing and represent serious medical problems both in the hospital and community setting. In this work a gelatin hydrogel modified with photo-cross-linkable methacrylamide groups at 10% concentration (GelMA10%), enriched with titanium dioxide nanoparticles (TiO_2NPs) and loaded with Neomycin Sulphate was developed with the aim to realize a tissue for wound care with improved mechanical and antimicrobial properties. TiO_2 nanocomposite GelMA films with two TiO_2NP concentrations were characterized to assess physicochemical, structural and mechanical properties by Scanning Electron Microscopy equipped with energy-dispersive X-ray spectrometer (SEM/EDX), micro-Computed Tomography (micro-CT) and X-ray Photoelectron Spectroscopy (XPS). Nanocomposite GelMA films showed more compact structure, reduced pore sizes and higher compressive modulus at the increasing NP concentration. They were able to absorb and retain water for prolonged time, however no significant differences in the swelling degree at the increasing of NP concentration were observed. In vitro drug release and antibacterial activity against *Staphylococcus aureus* of nanocomposite GelMA film enriched with 1 mg/ml of TiO_2NPs, identified as good candidate for wound healing, were investigated. Both GelMA and TiO_2 nanocomposite GelMA films loaded with drug exhibited a strong antibacterial action, whereas GelMA containing only TiO_2NPs did not show any antimicrobial properties.

Keywords: GelMA; TiO_2NPs; mechanical properties; structural characterization; drug release; antimicrobial activity; wound dressing

1. Introduction

Chronic wounds caused by burns, surgery and chronic diseases, such as diabetes, compromise the skin's immune and protective mechanisms; as a result, bacteria can easily infect the wound. Studies on microorganisms associated with wound infections showed that *Staphylococcus aureus* followed by *Pseudomonas* spp., and *Escherichia coli* are the most prevalent pathogen on the wound surface. *Staphylococcus aureus* represents the most common Gram-positive bacteria in wound infections [1].

Severe bacterial infections can delay the healing process by producing a biofilm, resulting in antibiotic resistance and therapeutic complications, such as chronic infections or septicaemias, which represent serious medical problems both in the hospital and community setting.

Traditional treatments of wound infections with antimicrobials and wound dressing with cotton wool, film, and cotton gauze showed some limitations such as inability to provide a moist

 doi:10.20944/preprints202603.2026.v1

environment around the wound and low resistance to bacterial infection [2]. Increasing demands have been made to develop no cytotoxic wound dressings with intrinsic antimicrobial properties, able to adsorb and remove the exudate, keep high moisture at the dressing-wound interface, allow gaseous exchange, provide thermal insulation. For these raisons, research on the development of hydrogel matrices has gained great interest in the scientific community. Hydrogels, composed of hydrophilic polymer networks, mimic natural tissue environments, enhancing cell viability and function. In wound healing, hydrogels provide a moist environment, promote cell migration and, due to their porous structure, enable the diffusion and delivery of bioactive agents and antibiotics, fostering skin regeneration and repair [3].

Gelatin hydrogel matrices, modified with photo-cross-linkable methacrylamide groups (GelMA) to obtain photopolymerizable hydrogels with polymeric networks like that of an extracellular matrix, have been extensively investigated by the scientific community for their characteristics of biocompatibility, biodegradability, stability, swelling capacity, ability to maintain a moist wound environment [4]. Moreover, the structural and swelling characteristics of hydrogel matrices make GelMA able to act as effective delivery vehicles for bioactive compounds, permitting the localized and sustained release of drugs. Neomycin sulphate is a broad-spectrum antibiotic, effective against infections due to certain Gram-positive bacteria, such as *Staphylococcus aureus* [5], and more efficient against most Gram-negative organisms such as *Proteus vulgaris, Escherichia coli, Aerobacter aerogenes, P. aeruginosa* etc. It is widely used in cutaneous formulations [6]. Due to its solubility in water and minimal systemic absorption, Neomycin sulphate represents a good drug to develop hydrogel for topical application [5,7].

However, low mechanical stiffness, toughness, large pore sizes of GelMA, which can lead to a burst release of the encapsulated therapeutics, strongly limit its biomedical application [8,9]. To overcome these limitations, different nanomaterials, such as such graphene oxide (GO) [10], gold [11], mesoporous silica nanoparticles [12] nanoclay [13] and carbon nanotubes (CNTs) [14], have been incorporated into different hydrogels.

Another nanomaterial used in the wound healing is titanium dioxide NPs (TiO_2NPs), due to its biocompatibility and antimicrobial properties. They have been incorporated or in situ generated into different polymer, such as chitosan, polyurethane membrane, gellan gum, showing that the enrichment with TiO_2NPs not only led to an increased mechanical stiffness and thermal stability but also to enhanced antibacterial properties [15–18].

In this study a TiO_2 nanocomposite gelatin hydrogel loaded with Neomycin sulphate for treating skin infections caused by *S. aureus* was developed. The mechanical strength provided from TiO_2NPs, and the use of Neomycin sulphate allow us to obtain a gelatin hydrogel with good structural characteristics, controlled drug release and improved antibacterial activity. The first phase of the research was devoted to the preparation and optimization of TiO_2 nanocomposite GelMA hydrogel films to be used as vehicle for the delivery of Neomycin sulphate. To obtain this goal, physicochemical, structural and mechanical characterization of GelMA films and polymeric films enriched with TiO_2NPs have been performed, as well as swelling properties and antibiotic release have been assessed. In the second phase of the study, the optimized TiO_2 nanocomposite GelMA film, loaded with antibiotic, was investigated for cell viability on human keratinocyte cells (HaCaT cells) and for antimicrobial properties on *S. aureus*.

2. Materials and Methods

TiO_2NP physico-chemical characterization

Titanium anatase nanoparticles with primary size <25 nm (TiO_2NPs)(Sigma-Aldrich Company Ltd., Gillingham,Dorset, UK), were characterized by Dynamic Light Scattering (DLS) (Zetasizer Ultra instrument, Malvern Instrument, UK) and SEM/EDX (FE-SEM Quanta Inspect, FEI Company, Eindhoven, Netherlands, equipped with Oxford EDS system) to determine their main physical-chemical characteristics: hydrodynamic diameter, primary size, shape, size distribution, agglomeration state, surface charge and chemical composition.

 doi:10.20944/preprints202603.2026.v1

TiO_2NPs were dispersed in Milli-Q water and the suspension was sonicated with a probe sonicator (Vibracell, Sonics & Materials Inc, Newtown, CT, USA, 750W, 20 kHz, 20% amplitude, 6.5 mm probe diameter) under temperature-controlled conditions for 13 min to reduce agglomeration. DLS measurements were performed on 1 ml of TiO_2NP suspension in Milli-Q deionized water. The temperature was set at 25 °C and two minutes were waited before starting the analysis to equilibrate the samples. Three determinations were performed on each sample. The number of readings for each determination and the duration of each measurement were automatically set by the instrument software. For particle size analysis, intensity distribution data were considered. For each sample, the mean value of the hydrodynamic diameter (Z-Average) and the polydispersity index (PDI) were determined, thus obtaining information on the stability and agglomeration state of the suspensions obtained. Zeta (ζ) potential measurements were also performed to determine the surface charge of TiO_2NPs. The measurements were conducted in triplicate by taking 750 µl from the suspensions and using an automatic protocol of the Zetasizer Ultra instrument.

To characterize TiO_2NPs by SEM/EDX, 0.5 ml suspensions were transferred onto polycarbonate filters with a diameter of 47 mm and a porosity of 50 nm. Portions of the obtained sample filters were mounted on SEM sample holders and coated with a thin Au film by cathodic sputtering. Sample analysis was performed by choosing a beam voltage of 20 KV. For each sample, more than one hundred particles were analysed and their shape and size were determined. EDX spectra were also acquired from the analysed particles to determine the elemental composition of the NPs and the presence of any impurities.

Preparation of TiO_2 nanocomposite GelMA film

To obtain the GelMA-based hydrogel film, 500 mg of lyophilized GelMA with 50% degree of methacrylation (PhotoGel 50% DS, CELLINK, Sweden, Gothenburg) were used, adopting a protocol slightly modified indicated by the manufacturer.

A PhotoInitiator (PI) solution was first prepared, containing 60 mg of Lithium phenyl-2,4,6-trimethylbenzoylphosphinate (LAP) photoinitiator in 12 ml of Dulbecco's Phosphate Buffer Solution (DPBS) (Sigma-Aldrich Company Ltd., Gillingham, Dorset, UK). The solution was first heated to 60 °C and kept in stirring, then filtered with a sterile 0.22 µm syringe filter and heated again to 60 °C to complete the dissolution. 5 ml of PI solution was added to the lyophilized GelMA, previously brought to room temperature to obtain polymeric films with a final GelMA concentration of 10% (GelMA10%). Starting from GelMA10% two nanocomposite films enriched with TiO_2NPs were made, one at a concentration 0.5 mg/ml, the other at 1 mg/ml of NPs, indicated as GelMA10%_0.5TiO_2NPs, GelMA10%_1TiO_2NPs, respectively.

Reconstituted GelMA with or without TiO_2NPs was placed on a rotating plate at 60 °C for 1 h to promote complete dissolution. pH was then checked to ensure that it was between 7 and 7.4. Two ml of each preparation were transferred into a cylindrical silicone mold, having a diameter of 2 cm and photocrosslinked with a UV lamp at 405 nm and 4 cm distance for 240 seconds.

Characterization of GelMA and TiO_2 nanocomposite GelMA film

After photocrosslinking hydrogel films with a diameter of 2 cm and a thickness of 0.5 cm were obtained. GelMA and TiO_2 nanocomposite films, were characterized from a physico-chemical and mechanical point of view by SEM/EDX, XPS, micro-CT and mechanical compression tests to study their morphology, the distribution of TiO_2NPs in the film, the film structure and the mechanical properties.

Moreover, swelling behaviour of GelMA and TiO_2 nanocomposite GelMA films was investigated.

Characterization by SEM/EDX analysis

To better understand the role of TiO_2NPs in the structure of GelMA-based films, cross-sections of freeze-dried samples of hydrogel films, at different photoinitiator concentrations, with and without NPs, were characterized by SEM/EDX. Films obtained after photocrosslinking were immersed for 24 h in DPBS to remove any non-crosslinked GelMA. After removing the DPBS, the samples were frozen in liquid nitrogen and freeze-dried for 24 h. The cross-sections of the freeze-dried samples were

 doi:10.20944/preprints202603.2026.v1

mounted on SEM stubs, coated with a thin Au film by sputtering and analysed by SEM at 20 KeV. Image editing was performed by Adobe Photoshop CS4 software (Adobe Systems, San Jose, CA, USA).

Characterization by XPS

Synchrotron Radiation-induced X-ray Photoelectron Spectroscopy (SR-XPS) was employed to investigate the surface chemical composition and electronic structure of GelMA and Neomycin sulphate-loaded GelMA PhotoGels. SR-XPS experiments were performed at the TEMPO beamline (SOLEIL Synchrotron, France) [19]. Spectra were collected in fixed analyser transmission mode with a pass energy of 10 eV, utilizing a monochromator grating of 800 l/mm (energy range 330–825 eV). Core levels (C1s, N1s, O1s, and S2p) were acquired at a photon energy (PE) of 560 eV, with an overall energy resolution of ΔE = 0.1 eV. Samples were prepared in the solid state by drop-casting an EtOH/H_2O (30:70 v/v) solution onto TiO_2/Si (111) wafer surfaces. The energy scale was calibrated by referencing the C1s aliphatic carbon signal to 285.0 eV [19]. Curve-fitting analysis was performed using Gaussian functions after the subtraction of a polynomial background [20,21]. To ensure physical consistency, a consistent fitting strategy, Full Width at Half Maximum (FWHM), was applied across all samples. For each core level, the same FWHM was imposed for all individual photoemission components. Calibration of the energy scale was made based on the C1s core level signal of aliphatic carbons, found at 285.0 eV [19]. All peaks were imposed to have the same full width at half maximum (FWHM) within each core level to ensure physical comparability. For core levels subjected to splitting, constraints on the areas were imposed to respect the branching ratio, which is 2:1 for the $S2p_{3/2,1/2}$ core levels. S2p spin-orbit splitting was imposed as 1.2 eV [20].

All atomic percentages are normalized to the total area of the corresponding element and therefore describe the relative distribution of chemical states, rather than absolute surface concentrations. Therefore, changes in relative percentages reflect chemical reorganization and screening effects, not simple additive behaviour.

Characterization by micro-CT

Characterization of tissue scaffolds is important for tissue regeneration, and it is crucial to characterize both the mechanical properties and the internal microstructure of the scaffolds [22,23].

Micro-CT is commonly used as 3D imaging methods that provide sufficient depth and resolution for life science studies such as scaffold visualization [24–26]. Long scanning time is not suitable for studies involving soft tissues, since motion artifacts may be introduced into images due to the deformation during the scans. In addition to the aforementioned limitations, another critical challenge in conventional absorption-based micro-CT is that it is difficult to visualize low-density materials, such as hydrogel, due to the low X-ray absorption attenuation of these materials [27].

Therefore, it was decided to freeze-dry the samples so that they could be analysed by microtomography and their internal structure could be studied. Morphological information, including internal structure, was obtained by micro-CT analysis performed on lyophilized samples using a high-resolution micro-CT scanner (Skyscan 1072; Bruker micro-CT, Kontich, Belgium). The resulting datasets were acquired at a resolution of 11.2 μm, with no filter, at a source voltage of 80 kV and a current intensity set at 124 μA, during a 180° sample rotation, with a rotation step of 0.45° and a frame exposure time of 1200 ms.

2D micro-CT images were processed by Adobe Photoshop CS4 software (Adobe Systems, San Jose, CA, USA) for editing.

Mechanical properties

To analyse the mechanical properties of the GelMA-based films and evaluate the influence of TiO_2 NPs, mechanical compression tests were performed on pure GelMA film and TiO_2 nanocomposite GelMA films using a Lloyd Instruments LR 30K dynamometer (Lloyd Instruments Ltd., Part of Ametek STC, West Sussex, UK) at room temperature. Cylindrical samples with a diameter of 2 cm and a thickness of 0.5 cm were prepared for the compression test. GelMA-based films have been incubated in DPBS for 24 h and kept at 37 °C. Before mechanical testing, the samples were then blotted dry and placed between two parallel plates, having a diameter of 5 cm; the

 doi:10.20944/preprints202603.2026.v1

compressive force was applied parallel to the longitudinal axis of the samples with a speed of 1.0 mm/min.

The compressive modulus was calculated as the slope in the linear region of the stress–strain curve corresponding to 0%–10% strain [28].

Swelling kinetics

GelMA-based and nanocomposite GelMA films obtained by photocrosslinking with UV lamp were weighed, obtaining the initial weight (w_0) of the films. Subsequently, they were soaked in DPBS and stored at 37 °C for 72 h. At intervals of 0.5, 1, 2, 4, 24, 48, and 72 h, they were removed from the DPBS, gently dried, and weighed, providing the weight (w_t) at different time intervals. From the difference in the weights obtained, we calculated the fluid absorption rate of each films using the following equation [29]:

$$Fluid\ absorption\ rate\ (\%) = \frac{w_t - w_0}{w_0} x100$$

The degree of swelling was presented as a percentage of the maximum weight obtained for each film, independently of time, with respect to the initial weight w_0. The assay was performed in triplicate and the results presented as the mean of experiments performed for each film.

GelMA and TiO_2 nanocomposite GelMA film loading

From morphological, mechanical and swelling data we choose the optimized GelMA and TiO_2 nanocomposite GelMA film formulations to prepare hydrogel loaded with Neomycin sulphate.

Neomycin was transferred in GelMA-TiO_2 reconstituted formulation containing PI solution, kept in stirring for 20 min at 60 °C. Two ml of preparation were transferred into a cylindrical silicone mold, and photocrosslinked, as above described, to obtain films containing 20 mg of Neomycin sulphate.

Drug release of GelMA and TiO_2 nanocomposite GelMA films

Standard curves of drug were obtained by using Ultraviolet visible spectrophotometer Lamda 35 (Perkin Elmer, Shelton, CT USA). Neomycin sulphate was tested at 310 nm. The amount of Neomycin sulphate released was obtained from the standard curve.

The optimized GelMA and GelMA nanocomposite films were weighed and placed into 4 ml of DPBS buffer solution (pH = 7.4). The samples were stored at 37 °C and at certain time intervals, 1 ml solution was taken out for UV-Vis measurements and 1 ml of fresh DPBS solution was added to the samples. According to the data, the mass and percentage of drug release were obtained.

Cytotoxicity test

To test the cytotoxicity of the nanocomposite films, MTT assay was performed according to EN ISO 10993-5 [30], using HaCat cells, a human skin cell line, obtained from ATCC (Manassas, USA). Cells were seeded into 96 well plates and cultured in DMEM supplemented with 10% FBS, for 24 h at 37 °C under 5% CO_2 atmosphere. The films were cut into 8 pieces (0.39 cm^2 area, 0.5 cm thick), sterilized under UV light for 30 min, and each piece added into DMEM supplemented with FBS to get extracts of the materials. The extraction was performed for 24 h at 37 °C. Cell culture medium was then removed, and extraction media obtained from the hydrogels at concentrations 100, 50, 25 and 12.5% were added to the cell monolayers. After cells were cultured for 24 h, 100 µL of MTT solution was added to each well after the removal of the extraction media, and the cells were further incubated in MTT solution for 3 h at 37 °C and 5% CO_2. In viable cells, MTT can be reduced into formazan crystals inside the cells by mitochondrial dehydrogenase enzymes. The resulting formazan formed inside the cells then were dissolved in DMSO and the blue-violet solution was quantified by measuring absorbance at 570 nm on a microplate reader (PerkinElmer, Boston, MA, USA). All materials' extracts were tested for six averages and data were collected from 3 independent experiments. Cell viability was expressed as percentage (%) compared to the control untreated cells (0% extract treatment).

Antibacterial activity

Antibacterial activity of GelMA films, unloaded or loaded with Neomycin sulphate, was determined by disk diffusion method and Time kill assay. *S. aureus* 6538p, a standard strain obtained from ATCC (Manassas, USA), was used in this study. Bacterial strain was inoculated on tryptone

 doi:10.20944/preprints202603.2026.v1

soya agar (TSA, Oxoid, Basingstoke Hampshire, UK) and incubated at 37 °C for 24 h. Subcultures were kept in trypticase soy broth (TSB) supplemented with 15% glycerol and stored at −80 °C for later use.

Disk diffusion test

The assay was conducted according to the Clinical and Laboratory Standards Institute (CLSI) guidelines [31] with slight modifications. A bacterial suspension with density corresponding to a McFarland 0.5 turbidity standard, which corresponds to 10^8 CFU/ml, was swabbed onto TSA plates with a sterile cotton swab. A piece of each GelMA films, corresponding to a 1/8 of the entire film disk (0.39 cm^2 area, 0.5 cm thick), was applied on each TSA plate, together with a sterile filter paper disc of 6 mm loaded with 20 µL of Neomycin sulphate solution (final concentration 30 µg) as positive control and a sterile filter disk loaded with TSB as negative control. Each plate was then incubated for 24 h at 37 °C. Each determination was performed in triplicate. The diameter of the inhibition zone produced by the bacterial strain representing antibacterial activity was measured in millimetres.

Time-killing growth curve

Time kill assay was performed with macro-dilution procedure according to the method recommended by CLSI [31] with slight modifications. Bacterial cells were cultured overnight and diluted to approximately 10^5 CFU/ml. A piece (0.39 cm^2 area, 0.5 cm thick) of each GelMA film, unloaded or loaded with the antibiotic, was added into the inoculum suspension. Muller Hinton Broth (MHB, Merk Life Science S.r.l., Milano) inoculated with each bacterial strain without test compound acted as the control in this experiment. The inoculum cultures were incubated at 37 °C. Samples (200 µl) were removed from each inoculum culture at time points 0, 1, 2, 4, 8, and 24 h and turbidity was recorded using a microplate reader (Perkin Elmer, Shelton, CT USA) at a wavelength of 600 nm. At the same time intervals, sample aliquots from each culture were ten-fold serially diluted and subcultured on Muller Hinton Agar (MHA, Merk Life Science S.r.l., Milano) plates. Viable counts were calculated in the units of CFU/ml and kill curves were plotted with time (h) against logarithm of the viable count (log10 CFU). Each experiment was carried out in triplicate.

Statistical analysis was conducted using one-way ANOVA followed by Tukey's post hoc pairwise tests (GraphPad Prism, Version 5.0). A p-value of less than 0.05 (* $p < 0.05$) was considered statistically significant.

3. Results and Discussion

3.1. TiO_2NP Characterization

The hydrodynamic diameters, polydispersity index and Zeta potential of 1 mg/ml and 0.5 mg/ml TiO_2NPs were determined. Results are shown in Table 1.

Table 1. DLS characterization of TiO_2NPs.

Concentration (mg/ml)	Z-Average (nm)	PDI	ζ potential (mV)
0.5	3700 ± 72	0.619 ± 0.117	-24.9 ± 0.6
1.0	3800 ± 513	0.785 ± 0.147	-34.0 ± 0.8

TiO_2NPs showed an agglomeration state that increased with increasing suspension concentration, as indicated by high PDI values. Size distributions confirmed that indicated by PDI values. The size distribution of the TiO_2NP suspensions at 0.5 mg/ml showed a maximum around 1.4 µm, that at 1 mg/ml highlighted the presence of two peaks of practically equal intensity, one around 894 nm, the other around 1.2 µm (Figure 1). Moreover, TiO_2NPs showed a negative surface charge (Table 1).

 doi:10.20944/preprints202603.2026.v1

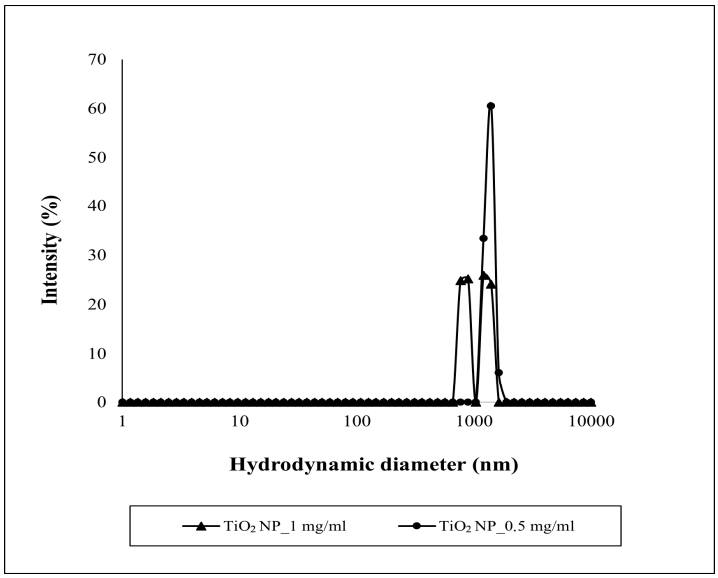

Figure 1. Size distributions by intensity of TiO_2NP suspensions.

SEM analysis displayed two main morphologies for TiO_2NPs: a spherical one, with an average diameter between 20 and 60 nm and an irregular one with a length of about 60 nm and a width of 40 nm. Size analysis by SEM confirmed what suggested on the TiO_2NP agglomeration state by the DLS data related to PDI. At the concentrations used in our study, the NPs form agglomerates (Figure 2A) whose diameter was between 65 and 1700 nm. At 0.5 mg/ml agglomerates smaller than 100 nm represent 19% of the analysed NPs. 65% of agglomerates had an average diameter between 100 and 400 nm (Figure 2B). At the concentration of 1 mg/ml only 14% of the agglomerates have dimensions smaller than 100 nm and 72% between 100 and 400 nm (Figure 2C).

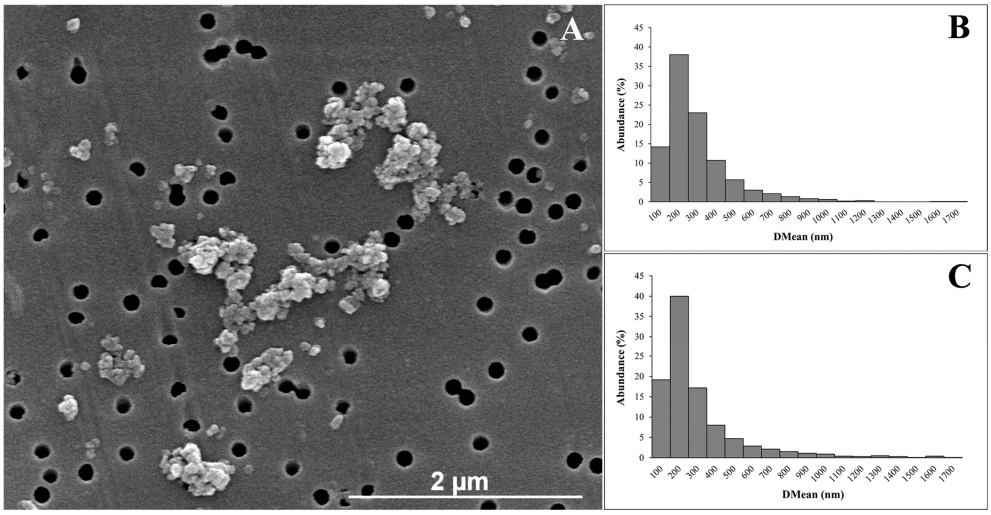

Figure 2. (A) morphology of TiO_2NPs; (B) size distribution of TiO_2NPs at 0.5 mg/ml obtained by SEM analysis; (C) size distribution of TiO_2NPs at 1 mg/ml obtained by SEM analysis.

3.2. GelMA Film Characterization by SEM/EDX Analysis

SEM observations of GelMA10% films showed an irregular and non-compact honeycomb structure with well-defined and largely no-interconnected pores with thin edges, indicating robust structural integrity (Figure 3A).

 doi:10.20944/preprints202603.2026.v1

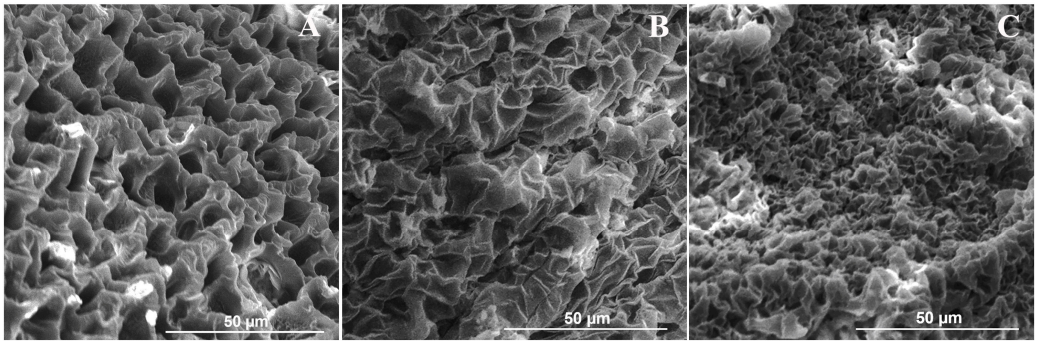

Figure 3. Morphology of GelMA and TiO_2 nanocomposite GelMA film cross section by SEM analysis: (A) GelMA10%; (B) GelMA10%_0.5TiO_2NPs; (C) GelMA10%_1TiO_2NPs.

Several other studies observed this porous network [8,32,33]. The mean diameter distribution of pores ranged from 8.6 to 41.6 µm, with an average value of 21.2 ± 9.0 µm. The addition of TiO_2NPs in GelMA hydrogel led to the formation of parallel planes and a more robust and highly homogeneous network structure with increased pore wall thickness (Figure 3B,C). This uniform honeycomb structure plays a crucial role in facilitating the efficient transport and sustained release of encapsulated drugs [34]. Moreover, morphological analysis showed a dependence of pore sizes on TiO_2NP concentration.

The mean diameter was between 9.1 and 36.6 µm with an average value of 20.7 ± 6.5 µm for GelMA10%_0.5TiO_2NPs, and between 7.0 and 24.4 µm with an average value of 13.5 ± 3.9 µm for GelMA10%_1TiO_2NPs. Morphological features exhibited by GelMA and GelMA-TiO2 nanocomposite films indicated their ability to support waste transfer. Moreover, the decrease of pore sizes observed in GelMA nanocomposite films suggest a higher crosslinking density at the increasing of TiO_2NP concentration and an increase in mechanical stiffness of hydrogel [8].

X-ray microanalysis spectra (Figure 4C) highlighted the presence of TiO_2NP small agglomerates both in the cross-sections of the GelMA-TiO_2NP nanocomposite films (Figure 4A), and on its surface (Figure 4B). Other studies observed hydrogel heterogenous and rough surface due to the agglomeration of TiO_2NPs [17,18].

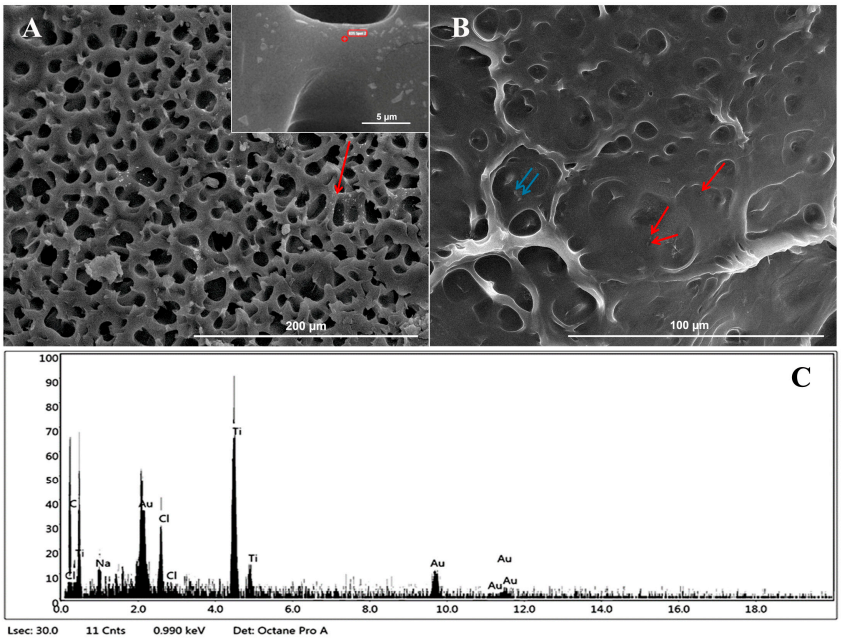

 doi:10.20944/preprints202603.2026.v1

Figure 4. SEM/EDX analysis of TiO_2 nanocomposite GelMA film: (A) SEM image of GelMA10%_1TiO_2NPs cross-section; (B) SEM image of GelMA10%_1TiO_2NPs surface; (C) Typical EDX spectrum of TiO_2NPs detected in GelMA.

3.3. XPS Analysis of GelMA and TiO_2 Nanocomposite GelMA_Neomicyn Sulphate Films

The chemical surface composition of GelMA films, deposited on TiO_2/Si (111) from an EtOH/H_2O (30:70) solution, was investigated via SR-XPS. This analysis served to characterize the pristine matrix, acting as a benchmark for monitoring spectral variations associated with the encapsulation of Neomycin sulphate. All measured spectra and spectral components individuated by applying a peak fitting procedure are shown in Figure 5.

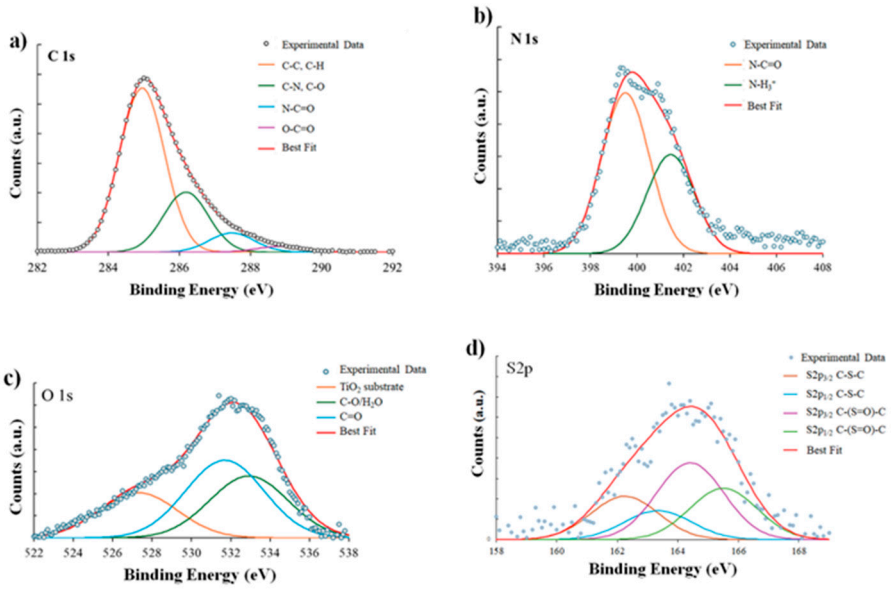

Figure 5. SR-XPS spectra collected on GelMA film: (a) C1s, (b) N1s, (c) O1s and (d) S2p core levels.

All binding energy (BE), full width half maximum (FWHM), atomic percentage values and proposed assignment are reported in Table S1 in the supporting information. C 1s spectrum is reported in Figure 5a. The envelope is broad and asymmetric, characteristic of the complex mix of amino acids and methacryloyl groups. The deconvolution identifies four distinct components: C-C at 285.0 eV BE, C-N and C-O at 286.18 eV BE, N-C=O at 287.5 eV BE and O-C=O at 289.1 eV BE.

The dominant component located at 285.0 eV BE, assigned to aliphatic C–C and C–H (66%) bonds, originating from the hydrocarbon side chains of amino acids as well as the methyl and vinyl functionalities introduced by the methacryloyl modification. Moving to higher binding energies, the contribute attributed to C–N and C–O (24.1%) at 286.2 eV BE, reflects the contributions of alpha-carbons (Cα) and peptide backbone linkages. The gelatine backbone is further characterized by the component at 287.5 eV BE, which corresponds to the amide carbonyls (N–C=O, 7.77%) of the peptide bonds connecting the amino acid sequence. Finally, the highest binding energy component at 289.5 eV BE is ascribed to carboxyl (O–C=O, 2.3%), resulting from the dual contribution of native carboxylic acid residues, and the methacrylate ester linkages formed during the functionalization process. It is noteworthy that all oxidized C signals are also affected by surface impurities, always observed in samples prepared in air from water solution [20].

N 1s spectrum (Figure 5b) shows two components: N-C=O at 399.5 eV BE and N-H3+ at 401.4 eV BE. The predominant component, at 399.5 eV BE (64.2%), is ascribed to amide nitrogen (N-C=O) atoms; this signal arises directly from the peptide bonds along the gelatine backbone, confirming the structural integrity of the protein matrix. A secondary contribution is observed at 401.2 eV BE (35.9%), which is attributed to protonated amine species N-H3+. This latter signal is indicative of the presence

 doi:10.20944/preprints202603.2026.v1

of unreacted side-chain amines, such as those found in lysine or arginine residues, which exist in a charged state likely due to zwitterionic interactions or surface effects with the underlying substrate.

The O 1s spectrum (Figure 5c) analysis focuses on the organic layer, explicitly excluding the lattice oxide component detected at 529.6 eV, which arises from the underlying TiO_2 substrate. Consequently, the organic oxygen contributions are resolved into two main components: the carbonyl oxygen (C=O) at 531.5 eV, associated with peptide amides and methacrylate esters, and the single-bonded oxygen (C–O) at 533.0 eV, attributed to hydroxylated residues.

Finally, Figure 5d shows the S 2p spectrum, which is characterized by the typical spin-orbit splitting doublet. The main S 2p3/2 component at 163.4 eV BE, the binding energy is consistent with thioether linkages (C–S–C). This is typical of methionine residues within the gelatine backbone and indicates that the sulphur atoms remain in their native, non-oxidized form. Additionally, a secondary contribution is observed at 164.5 eV, which can be attributed to oxidized methionine species (such as methionine sulfoxide). This indicates that while a significant portion of the sulphur atoms remains in their native, non-oxidized form, a detectable fraction has undergone partial oxidation.

Following the characterization of the supporting matrix, the SR-XPS study focused on the nanocomposite GelMA loaded with Neomycin sulphate to verify the drug's distribution and its chemical interplay with the polymer surface (Table S2 in the supporting information). The C 1s spectrum for the Neomycin sulphate-loaded sample is reported in Figure 6a.

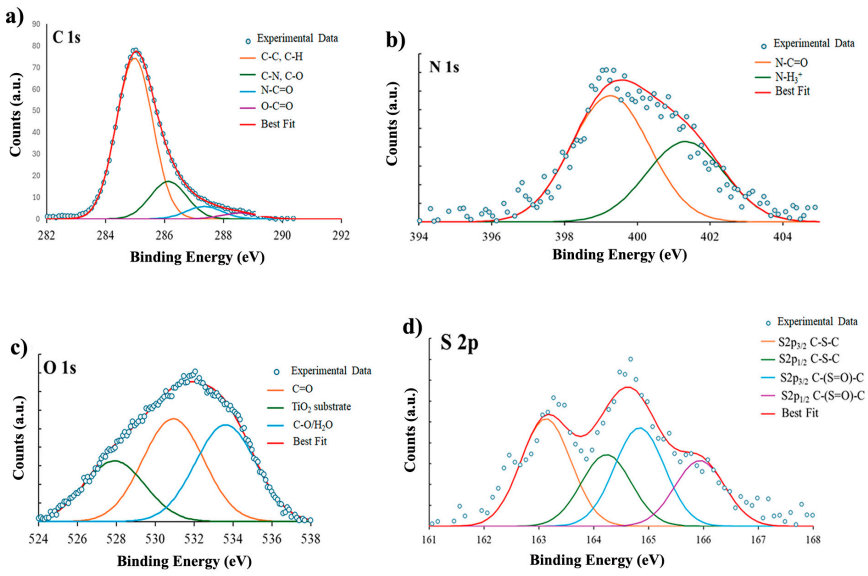

Figure 6. SR-XPS spectra collected on sample TiO_2 nanocomposite GelMA film loaded with Neomycin sulphate: (a) C1s, (b) N1s, (c) O1s and (d) S2p core levels.

The profile was deconvoluted into four chemically distinct environments, like the pristine matrix but with modified relative intensities, the most important difference between the two C1s spectra being the higher intensity of C-C component in Neomycin-loaded sample. Accordingly, the dominant signal at 285 eV BE (74.3%) is assigned to aliphatic C–C and C–H bonds. The component at 286.1 eV BE (17.3%) corresponds to C–N and C–O single bonds, while the peptide backbone amides (N–C=O) are identified at 287.3 eV BE (5.7%). The highest binding energy peak at 288.6 eV BE (2.7%) is ascribed to carboxyl and ester functionalities (O–C=O). N 1s spectrum (Figure 6b) reveals two main contributions, similarly to the pristine system. The primary component at 399.3 eV BE (60.2%) corresponds to the amide nitrogen (N–C=O) of the gelatine backbone. A significant secondary peak is observed at 401.3 eV BE (39.8%), attributed to protonated amine species ($N\text{-}H_3^+$). This fraction includes contributions from both the native lysine/arginine residues and the amino groups of the encapsulated Neomycin sulphate, and its relative intensity is increased with respect to the pristine sample, as expected. O 1s spectrum (Figure 6c) is deconvoluted into three distinct components. The

 doi:10.20944/preprints202603.2026.v1

signal at 527.9 eV BE (23.3%) arises from the lattice oxide (TiO_2) of the underlying substrate. The organic oxygen contributions are resolved into the carbonyl peak (C=O) at 530.9 eV BE (39.7%) and the single-bonded oxygen peak (C–O) at 533.6 eV BE (37.1%), associated with hydroxyl groups and retained water molecules. The S 2p spectrum (Figure 6d) confirms the presence of sulphur-containing residues, displaying two main contributions. The S 2p3/2 component at 163.1 eV BE is attributed to the thioether groups (C–S–C) of methionine, while the peak at 164.9 eV BE corresponds to the oxidized forms of methionine (sulfoxides). Although the overall profile remains similar to the pristine GelMA, a slight shift in the binding energies is observed.

Despite modulating the photon energy up to 1100 eV to increase the Inelastic Mean Free Path (IMFP) and enhance the sampling depth, no photoemission signal associated with the Ti 2p core level was detected. This suggests that the TiO_2 concentration remains below the instrumental sensitivity threshold, likely due to a low surface density of the nanoparticles and the significant photoelectron attenuation (screening effect) exerted by the thick organic GelMA/Neomycin sulphate overlayer.

The XPS data confirm the successful loading of Neomycin sulphate within the GelMA matrix, as primarily demonstrated by an increase in the relative area of the C–O species within the O 1s spectrum compared to the pure GelMA baseline. Regarding the interaction mechanism, no significant binding energy shifts were observed for the N 1s or C1s components, ruling out the formation of new covalent bonds. However, the retention of the drug within substrate, coupled with the increase in the protonated amine fraction ($-NH_3^+$), is consistent with a physical encapsulation driven by electrostatic interactions between the polycationic aminoglycoside and the anionic hydrogel network [35].

Furthermore, the broad spectral envelopes observed for the O 1s and S 2p core levels reflect the high structural complexity and the inherently amorphous nature of the functionalized hydrogel network, consistent with established characterizations of gelatine-based biomaterials [5]. In particular, the extensive hydrogen-bonding network established between the multiple hydroxyl residues of Neomycin sulphate and the GelMA peptide backbone, along with the presence of residual bound water, induces a continuum of slightly shifted electronic environments. Such spectral characteristics underscore the chemical heterogeneity of the system, where methionine residues and oxygen-containing functional groups experience a variety of micro-environments dictated by the disordered arrangement of the methacrylated protein chains and the drug-polymer interface [36].

3.4. Micro-CT Analysis of GelMA and TiO_2 Nanocomposite GelMA Films

Starting from TIFF images obtained in the microtomographic acquisition step, the NRecon (v. 1.7.0) and CTAn (v. 1.16) software (Bruker, Kontich, Belgium) were used to reconstruct the cross-sectional images and study the variation in the internal structure of the samples with varying amounts of TiO_2NPs, as shown in Figure 7.

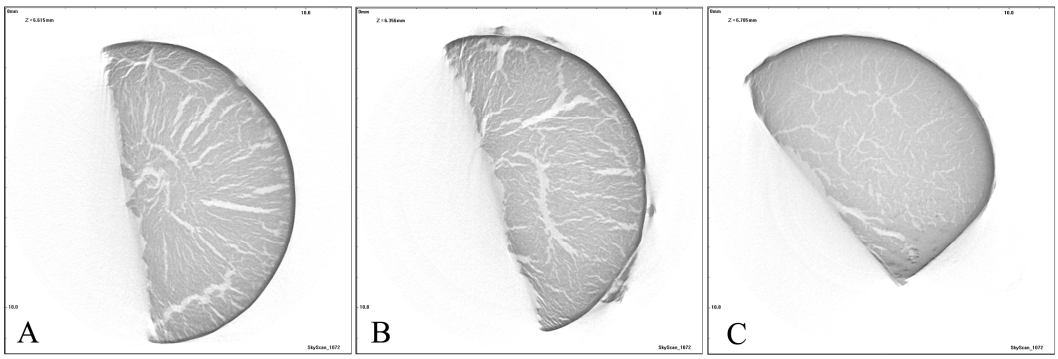

Figure 7. Micro-CT images of (A) GelMA10%; (B) GelMA10%_0.5TiO_2NPs; (C) GelMA10%_1TiO_2NPs.

From the images, it can be observed that, by increasing the amount of TiO_2NPs, the voids in the internal structure of GelMA10%_1TiO_2NPs were significantly reduced (Figure 7C). A smaller amount

 doi:10.20944/preprints202603.2026.v1

of voids gives the sample greater compressive strength and therefore prevents rapid drug release. Subsequently, for each of the three freeze-dried samples, a dataset of a Volume Of Interest (VOI), constrained in terms of size, was extracted. In CTAn, the VOIs were analysed through a procedure that included thresholding, noise reduction, and 3D analysis to determine and quantify the pore distribution within the three structures. The porosity values of GelMA10% and GelMA nanocomposites, confirmed that at the increasing of TiO_2NP concentration, the structure of GelMA10% became more compact. In fact the porosity of GelMA10% was 10.15%, while 12.26% and 5.11% for GelMA10%_0.5TiO_2NPS and GelMA10%_1TiO_2NPS respectively.

3.5. Mechanical Properties of GelMA and GelMA Nanocomposite Films

The mechanical properties of GelMA-based films were regulated by TiO_2NP concentration. Experimental data showed the compression modulus of GelMA10% reached the value of 4 kPa.

The compressive stress-strain curves revealed that the presence of nanofiller led to significant improvements in the mechanical strength of the nanocomposite samples (Figure 8); the presence of TiO_2NPs to a significant increase in compressive strengths for all the nanocomposite samples compared to the GelMA10% sample.

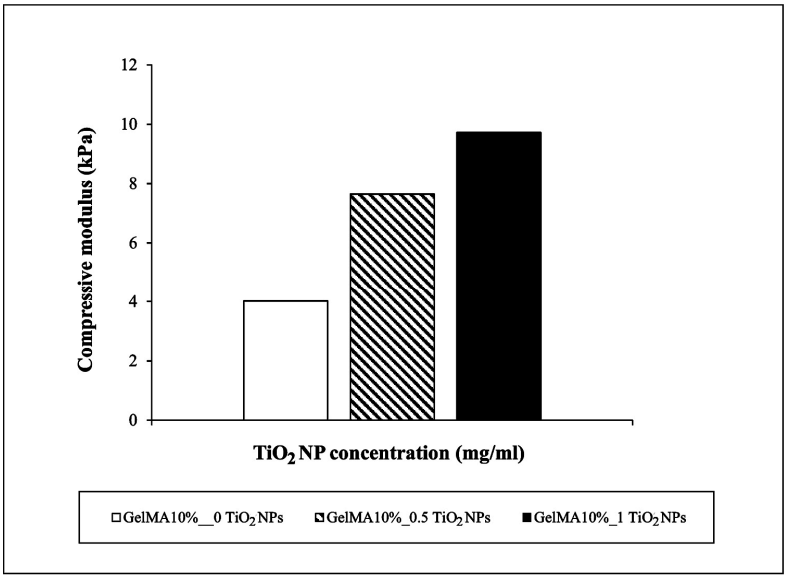

Figure 8. Effects of TiO_2NP concentration on compressive modulus of GelMA10%.

Enrichment of 1 mg/ml TiO_2NPs in GelMA10% led to a more than twofold increase in the compressive modulus. Also, Ismail et al. (2019) [17] showed an improvement of compressive modulus for gellan gum biofilm incorporating TiO_2NPs. The Authors suggest that high surface interaction between TiO_2NPs and biopolymer matrix leads to effective stress transfer between NP nanofiller and biopolymer chains.

3.6. Swelling Behaviour

A fundamental aspect for wound healing is the swelling behaviour of hydrogel films, since it determines the adhesion of the film to the wound, the ability to absorb exudates and finally the prolonged release of the encapsulated therapeutic treatments. Swelling behaviour of GelMA film and TiO_2 nanocomposite GelMA films are displayed in Figure 9.

 doi:10.20944/preprints202603.2026.v1

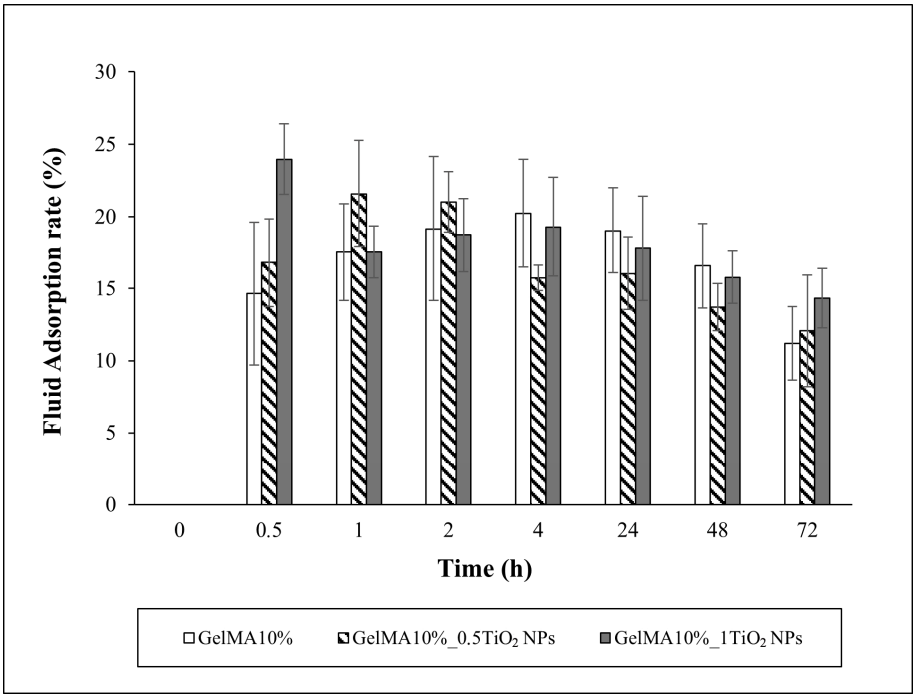

Figure 9. Swelling behaviour of GelMA and nanocomposite GelMA films.

GelMA10% films swelled up to 4 h then the fluide absorption rate started to slowly decrease probably due to polymeric erosion. The swelling of the films can be due to the hydrophilic nature of GelMA and the surface saturation that leads to the migration of water molecules into the film matrix, causing the chain expansion because of the weakening of the intramolecular hydrogen bonds [37]. The swelling degree of GelMA10% was 20.2% ± 3.7%. The addition of 0.5 mg/ml TiO_2NPs led to an increase of fluid absorption rate up to 2 h, while a burst increase after 0.5 h was observed for GelMA10% enriched with 1 mg/ml of TiO_2NPs. At 72 h GelMA10%_1TiO_2NPs exhibit a fluid adsorption higher than GelMA10%. No significant differences in GelMA10% film enriched with TiO_2NPs at the increasing of NP concentration were observed (Figure 9).

The swelling degrees of 21.6 ± 3.8% and 23.98 ± 2.4% for GelMA10%_0.5TiO_2NPs and GelMA10%_1TiO_2NPs respectively indicated a slight increase in swelling behaviour of GelMA enriched with TiO_2NPs, due to the hydrophilic nature of the anatase TiO_2NPs.

Conflicting data on the swelling behaviour of hydrogels incorporating TiO_2NPs are available in the literature. Ren et al. (2015) [38] showed an increased water binding capacity of PVA/xylan hydrogel enriched with TiO_2NPs. Higher swelling was also observed in gellan gum film incorporating TiO_2NPs. Authors suggested that the enrichment of TiO_2NPs contributed to the higher surface area/volume ratio of the film, facilitating the adsorption of water and TiO_2 molecules through the film [17]. In contrast, Gohargani at al. (2020) [39] demonstrated a significant decrease of swelling degree in biodegradable chitosan-whey protein-based film containing TiO_2NPs.

On the whole data indicated that GelMA10%_1TiO_2NP films were good candidate for wound healing due to their ability to absorb and retain water for prolonged time.

3.7. Neomycin Sulphate Release

A calibration curve was obtained, using antibiotic solutions at 370 μg/ml, 750 μg/ml, 1250 μg/ml, 2.5 mg/ml. The UV spectra of Neomycin sulphate showed a peak at 310 nm.

The calibration curves of antibiotic were $y=1.9549 \cdot 10^{-5}$ x -0.0074006, R= 0.99731. From the calibration curves we estimated the cumulative Neomycin sulphate release (Figure 10).

 doi:10.20944/preprints202603.2026.v1

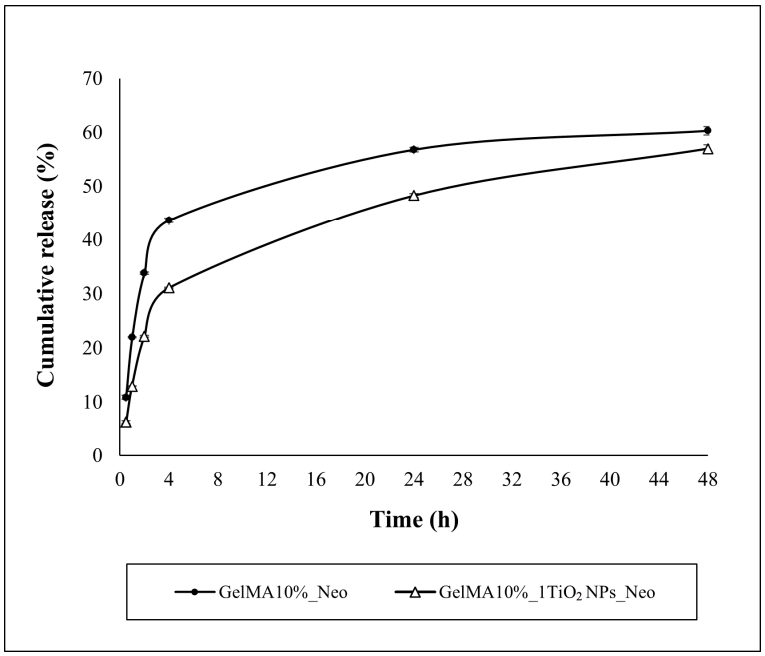

Figure 10. Cumulative Neomycin sulphate release of GelMA and TiO_2 nanocomposite GelMA films.

The process of Neomycin sulphate release showed three stages in GelMA10% films. A burst release of drug was observed in the first 4 h in which it can exert antibacterial action to protect the wound from secondary infection, followed by slower release between 4 and 24 h at which about 57% of antibiotic was released. After 24 h the slope of the cumulative drug release curve further decreased and about 68% of Neomycin sulphate was released. Three stages were observed also in the process of release for GelMA10% film enriched with 1 mg/ml of TiO_2NPs, but in each of three stages the release was slower than in GelMA10%. In the first stage (0-4 h) the slope of the cumulative release curve for TiO_2 nanocomposite GelMA film was lower than that observed for GelMA10%, whereas in the second was higher. This result agrees with the swelling behaviour of GelMA10% which swelled up to 4 h. The enrichment of 1 mg/ml TiO_2NPs did not affect significantly the swelling properties of GelMA film but the observed reduction in pore sizes led to reduced and slowed diffusion of Neomycin sulphate and increased entrapment of the drug within the hydrogel meshes, thus inducing a more controlled drug release. Overall, these data indicate that the addition of TiO_2NPs at a concentration of 1 mg/ml allowed us to obtain a controlled, sustained and prolonged release of Neomycin sulphate.

To understanding the release mechanism, the cumulative release profile of GeLMA10% and TiO_2 nanocomposite GelMA film enriched with 1 mg/ml of TiO_2NPs was fitted to Ritger–Peppas model:

$$\frac{M_t}{M} = kt^n$$

where M_t is the mass of drug released at time t, M the total mass of drug, k a kinetic constant, and n is the diffusional exponent. The k constant gives indication on the burst release of drug, while the diffusional exponent n which gives information on release mechanism depends on the type of hydrogel geometry and polymer polydispersity [40].

For GelMA10% film we obtained k=18.01 h^{-1} and n= 0.38, with R^2= 0.915. The diffusional exponent value obtained for our cylindrical geometry of hydrogel matrice suggests a pseudo fickian diffusion mechanism for GelMA10%, with a slow drug release [5]. While GelMA10% is highly porous, it acts with a "pseudo" Fick mechanism in which the relaxation of the GelMA polymer chains is very slow comparable to the solvent diffusion time, reducing the initial burst effect at <30% in the first two hours, followed by a sustained release. This behaviour is likely due to the polymer concentration, which has led to a relatively dense structure and a small free volume, and to the degree of cross-linking achieved, which makes the polymer chains difficult to separate. Also, Vigata et al. (2020) [41] observed a controlled release with a pseudo-Fick mechanism for GelMA10% concentration

 doi:10.20944/preprints202603.2026.v1

loaded with different doses of Abraxane. The Authors showed that GelMA10% significantly reduced the amounts of released drugs, increasing the sustainability of the release and the fraction of Abraxane released for all doses was not statistically different.

For GelMA10% enriched with 1 mg/ml of TiO_2NPs we obtained k= 11.86 h^{-1} and n = 0.46 with R^2= 0.931, indicating a lower burst release of Neomycin sulphate in GelMA nanocomposite The diffusional exponent values for geometry of hydrogel matrice suggests an anomalous transport phenomenon with comparable velocity of polymer chain relaxation and solvent diffusion, controlled by drug diffusion and erosion or relaxation of polymer chains [5]. This behaviour is probably due to higher crosslinking density achieved by the enrichment of hydrogel with TiO_2NPs which led to a reduced pore size of GelMA10% and further slowed down the diffusion-driven release.

3.8. Biocompatibility of GelMA and GelMA Nanocomposite Films

According to the UNI EN ISO guidelines, the extracts eluted from the hydrogel dressings were used as the original extract at 100% concentration and as dilutions of the original extract at 50%, 25%, and 12.5% (v/v). Cytotoxicity test results showed that the viability of cells treated with extracts at all concentrations was greater than 70% (Figure 11, dotted line), which represents the cut-off suggested by the guidelines for the absence of a cytotoxic effect. The tested hydrogels therefore have non-cytotoxic potential and can be considered cytocompatible.

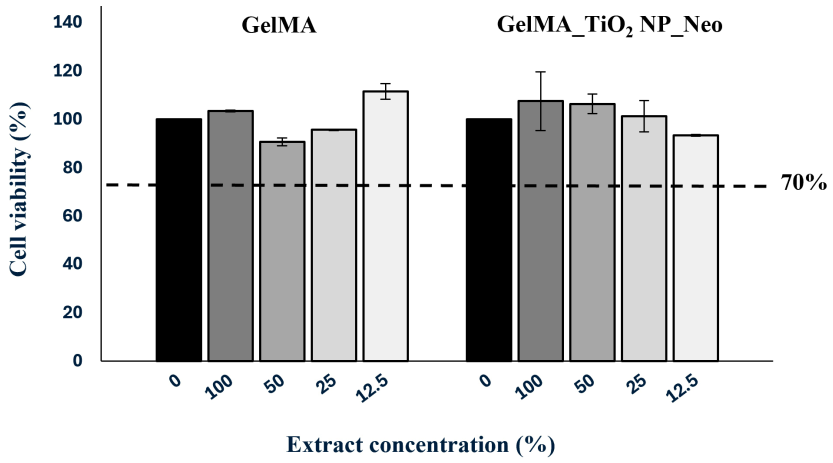

Figure 11. Cytotoxicity evaluation of hydrogel dressings on HaCat cell monolayers using MTT-based extract test.

3.9. Antibacterial Activity of Optimized Nanocomposite GelMA Films

To evaluate the antibacterial action of GelMA nanocomposites loaded with Neomycin sulphate and possible synergistic effect with TiO_2NPs, we tested optimized GelMA samples as following scheme: GelMA10% film and GelMa10% film loaded with Neomycin sulphate, GelMA10%_1TiO_2NP film and GelMA 10%_1TiO_2NP film loaded with Neomycin sulphate.

Disk diffusion test results indicated that GelMA and TiO_2 nanocomposite GelMA films loaded with Neomycin sulphate significantly inhibited the growth of *S. aureus*, compared to the blank control and GelMA films without antibiotics (Table 2). A comparable zone of inhibition for both GelMAs, with or without TiO_2NPs, loaded with the antibiotic, was evidenced, suggesting that the antibacterial activity was entirely due to the action of Neomycin sulphate, regardless of the TiO_2NPs embedded into gel dressing.

 doi:10.20944/preprints202603.2026.v1

Table 2. Disk diffusion test.

Samples	Zone of inhibition (mm)
Neomycin sulphate (30 µg)	14 ± 1
GelMA10%	0 ± 0
GelMA10%_Neomycin sulphate	25 ± 0.5
GelMA10%_1TiO2NPs	0 ± 0
GelMA10%_1TiO2NPs_Neomycin sulphate	24 ± 1.5

Optical density curves confirmed the action of the antibiotic loaded into GelMA and GelMA_1TiO2NP nanocomposites, with bacterial inhibition starting from 1 to the 24 h time interval (Figure 12A,B).

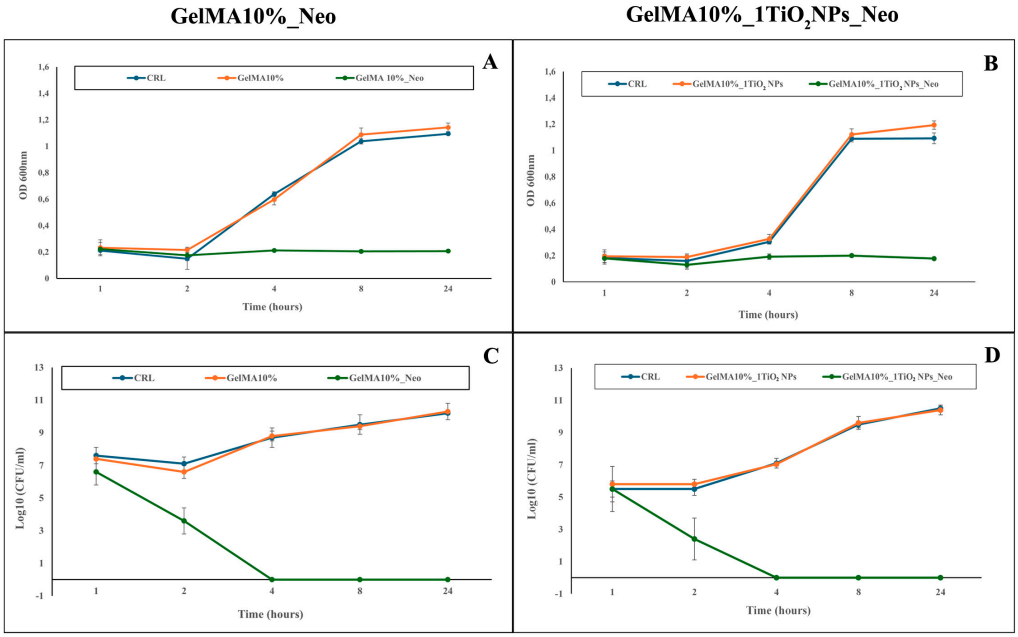

Figure 12. Effect of hydrogel specimens on the growth of *Staphylococcus aureus* 6538p strain under exposure to GelMA10% (A,C) and GelMA10%_1TiO2NPs (B,D) hydrogels, both unloaded and loaded with Neomycin sulphate.

Time kill assay evidenced that the Neomycin sulphate released during the first 4 h of bacterial growth was able to reduce bacterial population of about 6 log10, compared to control untreated sample and GelMA nanocomposites without Neomycin sulphate cultures (Figure 12C,D). GelMA nanocomposite made with TiO2NPs also in this assay showed antibacterial activity comparable to that of the GelMA nanocomposite without the nanoparticles, further confirming the absence of an antibacterial effect of TiO2NPs. In contrast with our data, other studies [17,18] observed antibacterial activity against both *S. aureus* and *E. coli* for gellan gum hydrogel incorporating green synthesised TiO2NPs. The lack of antimicrobial activity of GelMA incorporating only TiO2NPs observed in our study is likely due to the low content of NPs loaded in the hydrogel (2 mg in the entire film) compared to TiO2NP concentrations used by Ismail et al. (2019) and Su et al. (2025) [17,18]. Moreover, the film integrity displayed for 72 h, consistent with the high crosslinking density and low relaxation of the polymer chains of GelMA10%_1TiO2NP could prevent the NP release and subsequent antibacterial action. In addition, although the photo-crosslinking and film sterilization steps involving UV light should photoactivate the TiO2NPs with the production of free radicals, these are likely not sufficient to exert an antibacterial action in our model.

 doi:10.20944/preprints202603.2026.v1

4. Conclusions

In this study a nanocomposite hydrogel was developed using GelMA at 10% concentration, incorporating TiO_2NPs and loaded with Neomycin sulphate. Our results showed that the enrichment of GelMA with 1 mg/ml of TiO_2NPs led to several advantageous properties. Physical and chemical analysis showed a compact and porous structure with smaller pore sizes and higher photo-crosslinking density compared to GelMA10% hydrogel. The incorporation of TiO_2NPs into GelMA10% led to a significant improvement of mechanical properties and made GelMA10% a good candidate for wound healing due to its ability to absorb and retain water for prolonged time as indicated by swelling data. The XPS data confirm the loading of Neomycin sulphate in GelMA matrix, with extensive hydrogen-bonding network between the multiple hydroxyl residues of Neomycin sulphate and the GelMA peptide backbone, consistent with a physical encapsulation driven by electrostatic interactions between the polycationic aminoglycoside and the anionic hydrogel network. The enrichment of GelMA with 1 mg/ml of TiO_2NPs in GelMA10% film provided a controlled drug release profile, reducing burst release and extending the duration of drug availability. From the collective results it can be known that the optimized GelMA hydrogel with TiO_2NPs showed an excellent antibacterial ability. The amount of Neomycin sulphate released in the first 4 hours was sufficient to inhibit almost all bacteria and ensure prolonged inhibition, as is desirable for wound-healing dressing. The antibacterial action was exerted only by the antibiotic, while the TiO_2NPs had no effect. Overall, our data indicate that GelMA10%_1TiO_2NPs exhibit promising structural and functional characteristics to be used as a model for drug loading or combinations of drugs that act synergistically, with the aim of reducing the dose and avoiding drug resistance.

Supplementary Materials: The following supporting information can be downloaded at the website of this paper posted on Preprints.org, Table S1: BE (eV), FWHM (eV), atomic percentages (in the same signal) and proposed assignments for all measured signals related nanocomposite GelMA10% sample; Table S2: BE (eV), FWHM (eV), atomic percentages (in the same signal) and proposed assignments for all measured signals related to the Neomycin-loaded nanocomposite GelMA10% sample.

Author Contributions: Conceptualization, B.D.B and M.G.A; Methodology: B.D.B; data curation, validation and investigation, B.D.B, M.G.A and R.P; investigation, B.D.B, M.G.A, R.P., R.M, M.R. G.I, P.I, A.F., G.D.A., and G. D.A; Writing—original draft preparation, B.D.B, M.G.A, R.P. and M.R.; Writing—review and editing: B.D.B, M.G.A and R.P.; project administration, B.D.B.; funding acquisition, B.D.B. All authors have read and agreed to the published version of the manuscript.

Funding: BANDO RICERCA INDIPENDENTE ISS 2023 - Advanced polymeric films enriched with TiO2 NPs and Essential Oils to improve mechanical and antibacterial properties in manufacturing of dressing for wound treatment. Project code: ISS20-d631ffc090e5.

Conflicts of Interest: The authors declare no conflicts of interest.

References

1. Rivera P., Bello M.B., Brito G., Pichardo G., Cruz E., Blanco D. Therapeutic Efficacy of 2% Mupirocin in Managing Staphylococcus aureus and Streptococcus pyogenes Wound Infections. *Cureus* **2025**, 17(4): e82366. DOI 10.7759/cureus.82366
2. Zhou R., Zhang W., Zhang Y., Wu X., Huang J., Bo R., Liu M., Yu J., Li J. Laponite/lactoferrin hydrogel loaded with eugenol for methicillin-resistant Staphylococcus aureus-infected chronic skin wound healing. *J Tissue Viability* **2024**, 33(3):487-503. doi: 10.1016/j.jtv.2024.05.006.
3. Kaur H., Gogoi B., Sharma I., Das D.K., Azad M.A., Pramanik D.D., Pramanik A. Hydrogels as a Potential Biomaterial for Multimodal Therapeutic Applications. *Mol Pharm* **2024**, 21(10):4827-4848. doi: 10.1021/acs.molpharmaceut.4c00595
4. Zhang J., Liu C., Li X., Liu Z., Zhang Z. Application of photocrosslinkable gelatin methacryloyl in wound healing. *Front. Bioeng. Biotechnol*. **2023**, 11:1303709. doi:10.3389/fbioe.2023.1303709

 doi:10.20944/preprints202603.2026.v1

5. Bercea M., Plugariu I.A., Gradinaru L.M., Avadanei M., Doroftei F., Gradinaru V.R. Hybrid hydrogels for neomycin delivery: synergistic effects of natural/synthetic polymers and proteins. *Polymers (Basel)* **2023,** 15, 630. https://doi.org/10.3390/ POLYM15030630
6. Dallo M., Patel K., Hebert A.A. Topical antibiotic treatment in dermatology. *Antibiotics (Basel)* **2023**, 12, https://doi.org/10.3390/ANTIBIOTICS12020188
7. Choi J.S., Kim D.W., Kim D.S., Kim J.O., Yong C.S., Cho K.H., Youn Y.S., Jin S.G., Choi H.G. Novel neomycin sulphate-loaded hydrogel dressing with enhanced physical dressing properties and wound-curing effect. *Drug Deliv.* **2016**, 23, 2806–2812, https://doi.org/10.3109/10717544.2015.1089958
8. Jaiswal M.K., Xavier J.R., Carrow J.K., Desai P., Alge D., Gaharwar A.K. Mechanically Stiff Nanocomposite Hydrogels at Ultralow Nanoparticle Content. *ACS Nano*, **2016,** 10(1):246-56. doi: 10.1021/acsnano.5b03918
9. Zandi N., Dolatyar B., Lotfia R., Shallageh Y., Shokrgozar M.A., Tamjid E., Nasim Annabi N.A., Simchi A. Biomimetic nanoengineered scaffold for enhanced full-thickness cutaneous wound healing. *Acta Biomaterialia* **2021**, 124, 191–204. https://doi.org/10.1016/j.actbio.2021.01.029
10. Shin S.R., Aghaei-Ghareh-Bolagh B., Dang T.T., Topkaya S.N., Gao X., Yang S.Y., Jung S.M., Oh J.H., Dokmeci M.R., Tang X.S., Khademhosseini A. Cell-laden microengineered and mechanically tunable hybrid hydrogels of gelatin and graphene oxide. *Adv Mater*. **2013**, 25(44), 6385-91. doi: 10.1002/adma.201301082
11. Liu M., Huang P., Wang W., Feng Z., Zhang J., Deng L., Dong A. An injectable nanocomposite hydrogel co-constructed with gold nanorods and paclitaxel-loaded nanoparticles for local chemo-photothermal synergetic cancer therapy. *J. Mater. Chem. B* **2019**, 7, 2667–2677
12. Arvejeh P.M., Chermahini, F.A., Marincola F., Taheri F., Mirzaei S.A., Alizadeh A., Deris F., Jafari R., Amiri N., Soltani A. A novel approach for the co-delivery of 5-fluorouracil and everolimus for breast cancer combination therapy: Stimuli-responsive chitosan hydrogel embedded with mesoporous silica nanoparticles. *J. Transl. Med.* **2025**, 23, 382
13. Chen L.H, Liang N.W., Huang W.Y, Liu Y.C., Ho C.Y., Kuan C.H., Huang Y.F., Wang T.W. Supramolecular hydrogel for programmable delivery of therapeutics to cancer multidrug resistance. *Biomater Adv.* **2023**, 146:213282. doi: 10.1016/j.bioadv.2023.213282
14. Shin S.R., Jung S.M., Zalabany M., Kim K., Zorlutuna P., Kim S.B., Nikkhah M., Khabiry M., Azize M., Kong J., Wan K.T., Palacios T., Dokmeci M.R., Bae H., Tang X.S., Khademhosseini A. Carbon-nanotube-embedded hydrogel sheets for engineering cardiac constructs and bioactuators. *ACS Nano* **2013**, 7(3), 2369-80. doi: 10.1021/nn305559j
15. Li B., Zhang Y., Yang Y., Qiu W., Wang X., Liu B., Wang Y., Sun G. Synthesis, characterization, and antibacterial activity of chitosan/TiO_2 nanocomposite against Xanthomonas oryzae pv. oryzae. *Carbohydr Polym.* **2017**, 152, 825-831. doi: 10.1016/j.carbpol.2016.07.070
16. Chen Y., Yan L., Yuan T., Zhang Q., Fan H. Asymmetric polyurethane membrane with in situ-generated nano-TiO_2 as wound dressing. *J. Appl. Polym. Sci.* **2011**, 119 (3), 1532–1541. doi 10.1002/app.32813
17. Ismail N.A., Amin K.A.M., Majid F.A.A., Razali M.H. Gellan gum incorporating titanium dioxide nanoparticles biofilm as wound dressing: Physicochemical, mechanical, antibacterial properties and wound healing studies. *Mater Sci Eng C Mater Biol Appl* **2019**, 103:109770. doi: 10.1016/j.msec.2019.109770
18. Su Y., Zhu X., Xu G., Guan Z., Jiao W., Zhang Z., Sun Y., Wang C., Zhang R., Luo Q., Sui Y., Yusoff M., Razali MH. Green biosynthesis of titanium dioxide nanoparticles incorporated gellan gum hydrogel for biomedical application as wound dressing. *Front Chem.* **2025**, 17;13:1560213. doi: 10.3389/fchem.2025.1560213
19. Polack F., Silly M., Chauvet C., Lagarde B., Bergeard N., Izquierdo M., Chubar O., Krizmancic D., Ribbens M., Duval J.-P., Basset C., Kubsky S., Sirotti F., Garrett R., Gentle I., Nugent K., Wilkins S. TEMPO: A New Insertion Device Beamline at SOLEIL for Time Resolved Photoelectron Spectroscopy Experiments on Solids and Interfaces, *AIP Conference Proceeding* **2010**, 1234, 185–188. https://doi.org/10.1063/1.3463169
20. NIST X-ray Photoelectron Spectroscopy Database, NIST Standard Reference Database Number 20, National Institute of Standards and Technology, Gaithersburg MD, 20899), DOI: https://dx.doi.org/10.18434/T4T88K, (retrieved [February 20 2026])

 doi:10.20944/preprints202603.2026.v1

21. Amatori S., Lopez A., Meneghini C., Calcabrini A., Colone M., Stringaro A., Migani S., Khalakhan I., Iucci G., Venditti I., Battocchio C.Gold nanorods derivatized with CTAB and hydroquinone or ascorbic acid: spectroscopic investigation of anisotropic nanoparticles of different shapes and sizes. *Nanoscale Advances* **2023**, 5 (15), 3924-3933. https://doi.org/10.1039/d3na00356f
22. Alexa R.L., Iovu H., Trica B., Zaharia C., Serafim A., Alexandrescu E., Radu I.C., Vlasceanu G., Preda S., Ninciuleanu C.M., Ianchis R. Assessment of Naturally Sourced Mineral Clays for the 3D Printing of Biopolymer-Based Nanocomposite Inks. *Nanomaterials (Basel)*. **2021**, 11(3):703. doi: 10.3390/nano11030703. PMID: 33799601; PMCID: PMC8001953.
23. Li N, Duan X, Ding XF, Zhu N, Chen X. Characterization of hydrogel-scaffold mechanical properties and microstructure by using synchrotron propagation-based imaging. *J Mech Behav Biomed Mater*. **2025**,163, 106844. doi: 10.1016/j.jmbbm.2024.106844
24. Cheah C., Chua C., Leong K., Chua S. Development of a tissue engineering scaffold structure library for rapid prototyping. Part 1: investigation and classification. *Int. J. Adv. Des. Manuf. Technol*. **2003**, 21, 291–301. https://doi.org/ 10.1007/s001700300034, 10.1007/s001700300034
25. Rawson S.D., Maksimcuka J., Withers P.J., Cartmell S.H. X-ray computed tomography in life sciences. *BMC Biol.* **2020**, 18 (1), 21. https://doi.org/10.1186/s12915- 020-0753-2, 10.1186/s12915-020-0753-2
26. Clark J.N., Heyraud A., Tavana S., Al-Jabri T., Tallia F., Clark B., Blunn G.W., Cobb J.P., Hansen U., Jones J.R., Jeffers J.R.T. Exploratory Full-Field Mechanical Analysis across the Osteochondral Tissue-Biomaterial Interface in an Ovine Model. *Materials (Basel)* **2020**, 13(18):3911. doi: 10.3390/ma13183911
27. Ning L., Zhu N., Smith A., Rajaram A., Hou H., Srinivasan S., Mohabatpour F., He L., Mclnnes A., Serpooshan V., Papagerakis P., Chen X. Noninvasive Three-Dimensional In Situ and In Vivo Characterization of Bioprinted Hydrogel Scaffolds Using the X-ray Propagation-Based Imaging Technique. *ACS Appl Mater Interfaces*. **2021**, 13(22):25611-25623. doi: 10.1021/acsami.1c02297
28. Zhao X, Lang Q, Yildirimer L, Lin ZY, Cui W, Annabi N, Ng KW,Dokmeci MR, Ghaemmaghami AM, Khademhosseini A. Photo-crosslinkable gelatin hydrogel for epidermal tissue engineering. *Adv Healthc Mater* **2016**, 5, 108–118
29. Araujo T.F. and Silva L.P. The Utilization of Central Composite Design for the Production of Hydrogel Blends for 3D Printing. *Coatings* **2024**, 14, 1324. https://doi.org/10.3390/coatings14101324
30. UNI EN ISO10993-5 (2017). Biological evaluation of medical devices. Part 5: Tests for in vitro cytotoxicity. Milano: Ente Nazionale Italiano di Unificazione
31. CLSI. Performance Standards for Antimicrobial Susceptibility Testing. 30th Ed. CLSI supplement M100. Waine, PA: Clinical and Laboratory Standards Institute; 2020.
32. Wu Z. and Hong Y. Combination of the silver−ethylene interaction and 3D Printing to develop antibacterial superporous hydrogels for wound management. *ACS Appl. Mater. Interfaces* **2019**, 11, 33734−33747
33. Yang Z., Ren X., Liu Y. Multifunctional 3D printed porous GelMA/xanthan gum based dressing with biofilm control and wound healing activity. *Mater Sci Eng C Mater Biol Appl* **2021**,131:112493. doi: 10.1016/j.msec.2021.112493
34. Jiang Z., Shen C., Su K., Wang Y., Ma S., Xie J., Hu A., Hu J. An injectable gelatin methacryloyl hydrogel for long-term intraocular drug delivery of voriconazole. *Visual Neuroscience* **2026**, 43: e002 https://doi.org/10.48130/vns-0025-0028
35. Venditti I., Testa G., Sciubba F., Carlini L., Porcaro F., Meneghini C., Mobilio S., Battocchio C., Fratoddi I. Hydrophilic Metal Nanoparticles Functionalized by 2-Diethylaminoethanethiol: A Close Look at the Metal–Ligand Interaction and Interface Chemical Structure. *The Journal of Physical Chemistry C* **2017**, 121 (14), 8002-8013. https://doi.org/10.1021/acs.jpcc.7b01424
36. Yue K., Trujillo-de Santiago G., Alvarez M.M., Tamayol A., Annabi N., Khademhosseini A. Synthesis, properties, and biomedical applications of gelatin methacryloyl (GelMA) hydrogels, *Biomaterials* **2015**, 73, 254-271.https://doi.org/10.1016/j.biomaterials.2015.08.045
37. Mahmood H., Khan I.U., Asif M., Khan R.U., Asghar S., Khalid I., Khalid S.H., Irfan M., Rehman F., Shahzad Y., A.M., Younus A., Niazi Z.R., Asima M. In vitro and in vivo evaluation of gellan gumhydrogel films: Assessing the co impact of therapeutic oils and ofloxacin on wound healing. *International Journal of Biological Macromolecules* **2021**, 166, 483–495. https://doi.org/10.1016/j.ijbiomac.2020.10.206

 doi:10.20944/preprints202603.2026.v1

38. Ren J., Wang S., Gao C., Chen X., Li W., Peng F. TiO_2-containing PVA/xylan composite films with enhanced mechanical properties, high hydrophobicity and UV shielding performance. Cellulose **2015**, 22 (1), 593–602
39. Gohargani M., Lashkari H., Shirazinejad A. Study on Biodegradable Chitosan-Whey Protein-Based Film Containing Bionanocomposite TiO_2 and Zataria multiflora Essential Oil. *Journal of Food Quality* **2020**, 8844167, 11 pages, https://doi.org/10.1155/2020/8844167
40. Li J., Mooney D.J. Designing hydrogels for controlled drug delivery. *Nat Rev Mater*. **2016**, 1(12):16071. doi: 10.1038/natrevmats.2016.71
41. Vigata M., Meinert C., Pahoff S., Bock N., Hutmacher D.W. Gelatin Methacryloyl Hydrogels Control the Localized Delivery of Albumin-Bound Paclitaxel. *Polymers (Basel)* **2020**, 12(2):501. doi: 10.3390/polym12020501